catalysts

MDPI

Article

An Alumina-Supported Ni-La-Based Catalyst for Producing Synthetic Natural Gas

Daniel E. Rivero-Mendoza [1], Jessica N. G. Stanley [2], Jason Scott [2] and Kondo-François Aguey-Zinsou [1,*]

[1] MERLIN Group, School of Chemical Engineering, The University of New South Wales, Sydney, NSW 2052, Australia; d.riveromendoza@aquahydrex.com

[2] Particles and Catalysis Research Group, School of Chemical Engineering, The University of New South Wales, Sydney, NSW 2052, Australia; jessica.stanley@unsw.edu.au (J.N.G.S.); jason.scott@unsw.edu.au (J.S.)

* Correspondence: f.aguey@unsw.edu.au; Tel.: +61-29-385-7970

Academic Editor: Rajendra S. Ghadwal
Received: 21 September 2016; Accepted: 25 October 2016; Published: 31 October 2016

Abstract: $LaNi_5$, known for its hydrogen storage capability, was adapted to the form of a metal oxide-supported (γ-Al_2O_3) catalyst and its performance for the Sabatier reaction assessed. The 20 wt % La-Ni/γ-Al_2O_3 particles were prepared via solution combustion synthesis (SCS) and exhibited good catalytic activity, achieving a CO_2 conversion of 75% with a high CH_4 selectivity (98%) at 1 atm and 300 °C. Characteristics of the La-Ni/γ-Al_2O_3 catalyst were identified at various stages of the catalytic process (as-prepared, activated, and post-reaction) and in-situ DRIFTS was used to probe the reaction mechanism. The as-prepared catalyst contained amorphous surface La–Ni spinels with particle sizes <6 nm. The reduction process altered the catalyst make-up where, despite the reducing conditions, Ni^{2+}-based particles with diameters between 4 and 20 nm decorated with LaO_x moieties were produced. However, the post-reaction catalyst had particle sizes of 4–9 nm and comprised metallic Ni, with the LaO_x decoration reverting to a form akin to the as-prepared catalyst. DRIFTS analysis indicated that formates and adsorbed CO species were present on the catalyst surface during the reaction, implying the reaction proceeded via a H_2-assisted and sequential CO_2 dissociation to C and O. These were then rapidly hydrogenated into CH_4 and H_2O.

Keywords: Sabatier reaction; lanthanum nickel; catalysis

1. Introduction

Fossil fuels such as oil, coal, and natural gas have and continue to be the primary means employed to meet society's energy needs. A key downside in relying on these carbon-rich compounds has been the accompanying increase in atmospheric CO_2 levels, from ~290 ppm in pre-industrial days to ~395 ppm in 2013, which is seen as the major culprit behind climate change [1,2]. Growing awareness of the impact anthropogenic CO_2 emissions have on global warming and the detrimental consequences further increases may bring has resulted in a need for reducing/capping these emissions [1,3,4]. The magnitude of the CO_2 emissions calls for the application of a portfolio of strategies and technologies to approach the reduction/capping task, from which converting the otherwise wasteful CO_2 into added value products including synthetic fuels, chemicals, and raw materials is particularly interesting assuming that the needed energy comes from renewables.

As a mitigation strategy, using CO_2 as a feedstock is based on the possibility of storing this compound in manufactured products and therefore preventing it from being released into the atmosphere. Functionality, abundance, renewable nature, and environmental friendliness are some of the features that make CO_2 an attractive C_1 building block for synthesis products such as paraffin,

dimethyl ether, methanol, higher alcohols, and formic acid [3,4]. Nowadays, CO_2 is employed in the production of urea, salicylic acid, and polycarbonates at an industrial scale [5], consuming altogether ~10 Mt of CO_2 y^{-1} as of 2007 [6]. However small this rate may seem compared to the ~35 BMt of CO_2 y^{-1} emitted in 2013, it only accounts for those few applications which have commercial status and hence represents a minute portion of its real mitigating potential. One application which could be deployed at a scale that would significantly contribute to the reduction of CO_2 emissions is the production of synthetic fuels through direct hydrogenation [3]. Holding great potential among the direct conversion processes is the Sabatier reaction (1):

$$CO_2 + 4H_2 \rightarrow CH_4 + H_2O \quad (1)$$

The main advantage behind the Sabatier reaction is its favourable thermodynamics and theoretical capability to reach high conversions at ambient conditions [7]. However, the stability of the fully oxidised CO_2 molecule and the eight-electron process its reduction entails set considerable kinetic limitations that hinder the performance of the process at mild operating conditions [3,4,7]. Thus, using a highly efficient catalyst is required to fully exploit the potential of the Sabatier reaction. Most of the research conducted in this field has dealt with the use of Ni-based catalysts [3,4,7–11], although other transition (e.g., Fe and Co) [9,12] and noble (e.g., Rh, Pt, Ru and Pd) [12–16] metal based systems have also proven active.

While more commonly associated with H_2 storage applications, bulk $LaNi_5$ has exhibited promising activity/selectivity for the Sabatier reaction [17–19]. For instance Ando et al. achieved CO_2 conversions of 92% and methane selectivity of 98% (achieved after a 5 h induction period) for bulk $LaNi_5$ (prepared by arc-melting) at 250 °C with a high reactants pressure of 5 MPa [18]. The bulk $LaNi_5$ was far superior to a mixed Ni_5LaO_x oxide, prepared by co-precipitation, which exhibited 8% CO_2 conversion after 5 h under the same reaction conditions.

The work reported here takes $LaNi_5$ and adapts it to a metal oxide-supported (γ-Al_2O_3) catalyst system where its performance for the Sabatier reaction is assessed. Changes in the La-Ni/γ-Al_2O_3 catalyst structure invoked by the initial activation step and the ensuing reaction process were examined in detail. In-situ DRIFTS analyses were performed to establish the nature of the surface species generated over the course of the reaction and provide insights into the Sabatier mechanism.

2. Results and Discussion

2.1. As-Prepared Catalyst (P_LaNi/Al)

ICP–OES gave the La-Ni loading and La/Ni molar ratio in P_LaNi/Al to be 18.3 and 4.5 wt %, respectively. The XRD pattern of P_LaNi/Al, as shown in Figure 1, exhibited reflections similar to those found in the pristine support, which corroborated the presence of poorly crystalline γ-Al_2O_3 (JCPDS 086-1410) and revealed a signal (centred at 2θ = 43.6°) corresponding to the stainless-steel (JCPDS 033-0397) sample holders used in the analyses. No additional features were observed in the XRD pattern of the P_LaNi/Al sample, where the absence of La- and Ni-related reflections suggested that these components were present either as amorphous phases or as small crystalline structures indiscernible by this technique.

Considering the aforementioned, La was assumed to be present as highly-dispersed, amorphous La_2O_3 at the surface of the P_LaNi/Al. In contrast, nickel in P_LaNi/Al was presumed to have formed Ni-Al surface spinels since the occurrence of such species in Ni/Al systems is widely known [19–24]. According to Li et al. the absence of XRD lines corresponding to these surface spinels results from their short-range three-dimensional order, provided that Ni ions only diffused into the first few outer layers of the Al_2O_3 support during their 450 °C calcination stage [22].

SEM imaging of P_LaNi/Al (Figure 2a) revealed an irregular surface comprising superimposed slab-like features and sub-micrometric aggregates (ca. 200–600 nm) which were evenly distributed across the micron-sized catalyst particles. TEM analysis of P_LaNi/Al (Figure 2b) revealed the presence

of small, evenly distributed particles with a diameter ranging from 1 to 6 nm (Table 1), which were discernible from the prevailing γ-Al_2O_3 support by their darker tone. These particles likely correspond to La- and Ni-containing deposits, but their exact make-up could not be defined.

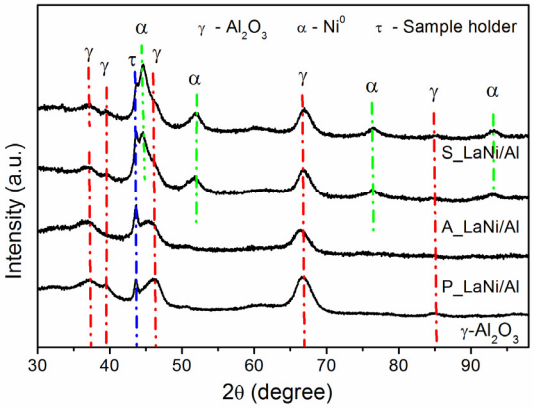

Figure 1. XRD patterns of the pristine γ-Al_2O_3 and the La-Ni/γ-Al_2O_3 catalyst as-prepared via SCS (solution combustion synthesis) (P_LaNi/Al), reduced under H_2 at 700 °C (A_LaNi/Al), and after 3 h of CO_2 hydrogenation at 400 °C (S_LaNi/Al).

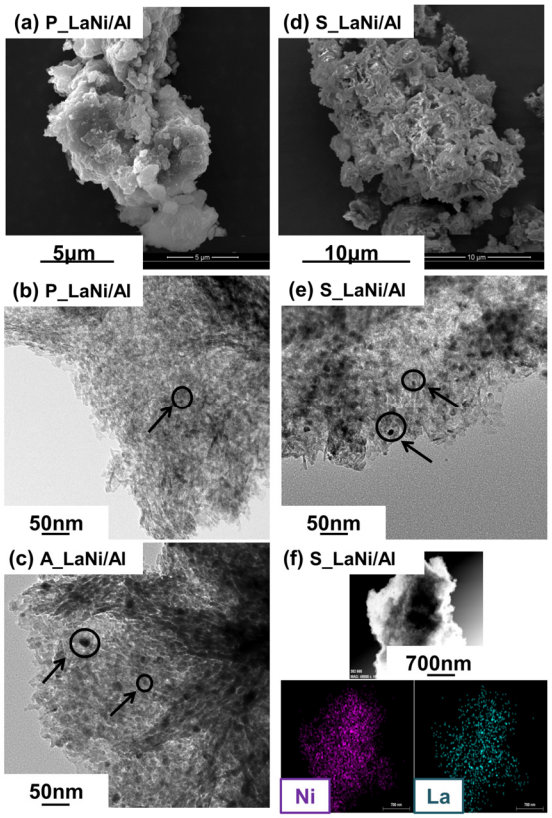

Figure 2. (**a**) SEM; and (**b**) TEM images of the La-Ni/γ-Al_2O_3 catalyst as-prepared via SCS (P_LaNi/Al); (**c**) reduced under H_2 at 700 °C (A_LaNi/Al); and (**d**) SEM; (**e**) TEM images and (**f**) associated elemental mapping after 3 h of CO_2 hydrogenation at 400 °C (S_LaNi/Al). Black arrows indicate La- and/or Ni particles.

Table 1. Average particle and Ni crystallite sizes (including degree of Ni dispersion) as estimated from TEM, XRD and pulsed H_2 chemisorption for the P_LaNi/Al, A_LaNi/Al, and S_LaNi/Al materials.

Materials	Particle Size (nm)	Ni Crystallite Size (nm)	
	TEM	XRD	H_2 Pulse (% Disp.)
P_LaNi/Al	1–6	-	-
A_LaNi/Al	4–20	5	37 (2.58)
S_LaNi/Al	4–9	6	-
Ni/Al	-	-	41 (2.36)

The H_2-TPR profile of P_LaNi/Al (Figure 3) revealed the presence of three reduction bands within two major reduction zones at temperatures across the range of 290–750 °C. The low-temperature zone between 290 and 425 °C contained a symmetrical band centred at 320 °C attributed to the reduction of amorphous NiO on the catalyst surface [22,25–27] since no nitrates from the SCS were expected to remain after calcination at 500 °C [28]. The peak at 583 °C was ascribed to octahedrally coordinated Ni^{2+} species (i.e., Ni^{2+}_{OC}) embedded in the crystalline structure of the γ-Al_2O_3 support [24,27,28], which concurs with the formation of surface Ni-Al spinels. The small shoulder at 695 °C was assigned to the reduction of Ni^{2+} species, either tetrahedrally coordinated (i.e., Ni^{2+}_{T}) in the crystalline structure of the support as per previous reports [22,27], or in La–Ni–Al containing species derived from the strong interaction between La and Ni ions [26]. The former interpretation stems from the widely accepted perception that Ni^{2+}_{T} species are more difficult to reduce than Ni^{2+}_{OC} ones [23,27], while the latter coincides with experimental observations from studies dealing with the promotion effects of La on Ni-based catalysts [26].

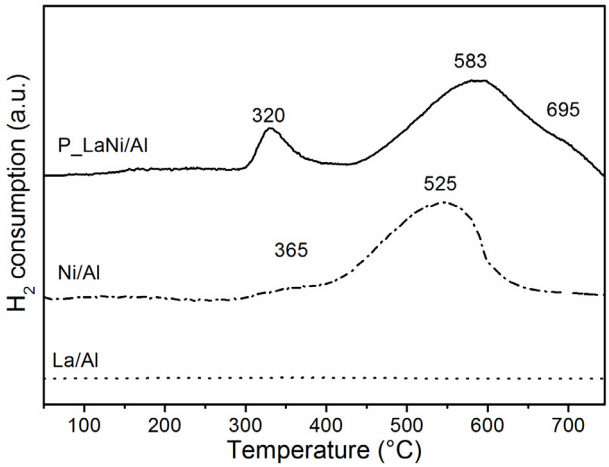

Figure 3. H_2-TPR profiles of La deposited on γ-Al_2O_3 (La/Al), Ni deposited on γ-Al_2O_3 (Ni/Al), and the as-prepared La-Ni/γ-Al_2O_3 (P_LaNi/Al).

Additional H_2-TPR analyses of Ni/Al (12.5 wt %) and La/Al (6.4 wt %) were conducted to assist with interpretation of the P_LaNi/Al profile (Figure 3). No reducible phases were observed in the La/Al sample, agreeing with the known irreducible nature of La oxides below 1000 °C [26,29]. However, the Ni/Al sample exhibited two reduction peaks including a broad shoulder-like feature at 365 °C and a peak centred at 583 °C. Similar to P_LaNi/Al, the low-temperature feature was attributed to surface NiO while the higher temperature peak was attributed to Ni^{2+}_{OC} species. The absence of a higher temperature shoulder, in conjunction with the absence of La in Ni/Al, infers that the 695 °C shoulder in the P_LaNi/Al H_2-TPR profile originates from the reduction of La–Ni–Al species and not from Ni^{2+}_{T} species. Additionally, the more prominent bulk NiO peak exhibited by the P_LaNi/Al sample indicates that La promoted the formation of the bulk-like NiO on the γ-Al_2O_3 support.

The XPS spectrum of the P_LaNi/Al sample was examined at the overlapping Ni2p/La3d, C1s, Al2p, and O1s regions to establish the surface chemical characteristics of the as-synthesised material. Analysis of the C1s region of the P_LaNi/Al spectra gave a C/Al atomic ratio of 0.11 (Supplementary Materials, Figure S1; Table S1), indicating that no substantial residual carbon remained on the catalyst surface after synthesis.

Peaks relating to the Ni and La species were extracted from the de-convoluted spectra (Supplementary Materials, Figure S2) and are shown in Figure 4a,b, respectively, with values for the relative amounts of each species provided in Table 2. Within Figure 4a the peaks at 856.49 and 862.72 eV for P_LaNi/Al correspond to the primary and shake-up lines of octahedrally coordinated Ni (Ni^{2+}_{OC}) in nickel-alumina spinels, respectively [21,23,27,30]. According to Poncelet et al., enhanced reducibility in Ni/Al observed at high Ni loadings is associated with octahedral nickel (Ni^{2+}_{OC}) species which resemble NiO [23]. These species would account for the low temperature reduction peak in the P_LaNi/Al TPR profile, provided that no bulk NiO signals (i.e., ca. 854.24 eV) [26] were observed from the XPS spectrum. No signals attributable to Ni^{2+}_{T} (i.e., at 858.1 eV) [23] were observed in the P_LaNi/Al XPS spectra, corroborating the H_2-TPR findings which suggested suppression of these species in the presence of La. The signals observed at 835.86 and 839.43 eV are attributed to the main and satellite peaks of La^{3+} from La_2O_3 dispersed on γ-Al_2O_3 [18,26,31].

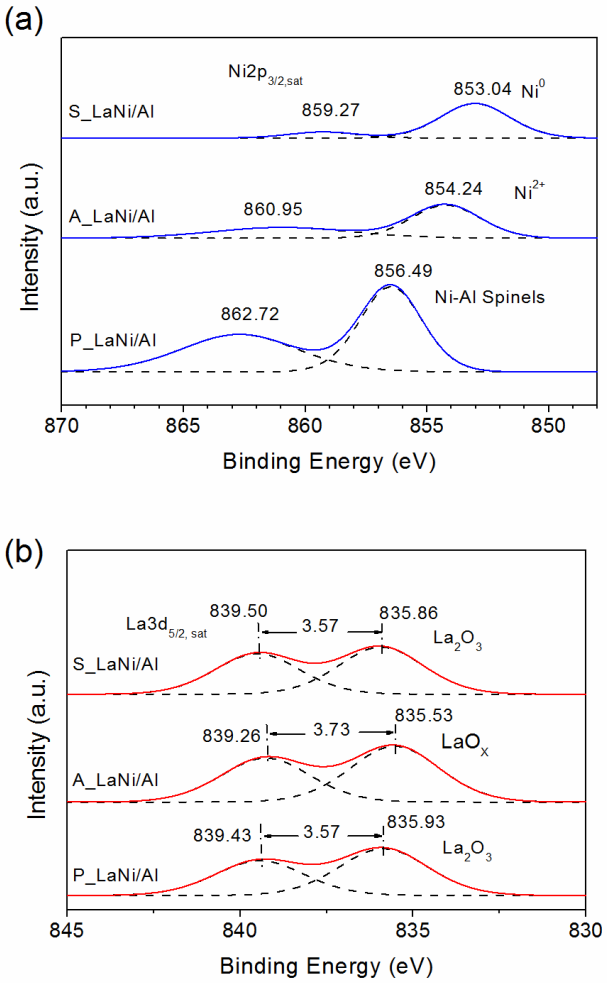

Figure 4. Deconvoluted XPS spectra for (**a**) Ni and (**b**) La species on the surface of the P_LaNi/Al, A_LaNi/Al, and S_LaNi/Al materials.

Table 2. Binding energies (BE) of core electrons, surface species and relative atomic ratios for Ni and La in the P_LaNi/Al, A_LaNi/Al, and S_LaNi/Al materials.

Materials	$Ni2p_{3/2}$ (Sat)			$La3p_{5/2}$ (Sat)		
	BE (eV)	Species	Ni/Al	BE (eV)	Species	La/Al
P_LaNi/Al	856.49 862.72	Ni-Al surface spinels	0.081	835.86 839.43	La_2O_3	0.022
A_LaNi/Al	854.24 860.95	Ni^{2+}	0.028	835.53 839.26	LaO_x	0.022
S_LaNi/Al	853.04 859.27	Metallic Ni	0.029	835.93 839.50	La_2O_3	0.020

The Al2p and O1s regions of the P_LaNi/Al XPS spectrum (Supplementary Materials, Figure S3) exhibited single peaks centred at 75.17 and 531.75 eV, respectively, which corresponded to the reported binding energies for Al_2O_3 [26,32]. These results diverge from the 74.0 eV (Al2p) and 830.8 eV (O1s) expected for bulk $NiAl_2O_4$ [33], implying the support surface remained essentially as alumina.

2.2. Reduced Catalyst (A_LaNi/Al)

The XRD pattern of the reduced catalyst (Figure 1) exhibited diffraction lines corresponding to the γ-Al_2O_3 support and the stainless-steel sample holder used for the analysis. Typical metallic nickel (JCPDS 001–1260) diffraction peaks were also observed with the Ni crystallite size estimated to be of 5 nm from the Scherrer equation (Table 1). No distinct $LaNi_5$ diffraction lines were observed for the A_LaNi/Al material as $LaNi_5$ formation from the corresponding metallic oxides has been reported to occur at temperatures >1000 °C [29,34,35].

SEM imaging of the A_LaNi/Al revealed a morphology akin to that of P_LaNi/Al. Clearly distinguishable nanoparticles were observable by TEM (Figure 2c), which were uniformly scattered across the γ-Al_2O_3 support and had diameters ranging between 4 and 20 nm. The majority of the deposits were observed to have diameters at the lower end of the size range, coinciding with the average Ni crystallite size determined from XRD. EDS elemental mapping (Supplementary Materials Figure S4) revealed even La and Ni dispersions across the catalyst surface, which suggests that the deposits comprise both Ni and La.

From the H_2-TPR profiles (Figure 3), the conditions used to activate the catalyst (700 °C under pure H_2) were expected to reduce all the nickel species present on Ni/Al and the majority of the nickel species on P_LaNi/Al. However, a minor portion of the nickel in the form of the La–Ni–Al component on P_LaNi/Al may have remained in an oxidised state. The average crystallite size of Ni and dispersion from the pulsed H_2 adsorption experiments for the reduced catalysts are given in Table 1. Both the A_LaNi/Al and Ni/Al samples exhibited a relatively low degree of Ni dispersion (<2.6%) as can occur for catalysts with a high Ni content [26]. A slightly higher Ni dispersion and concomitant lower crystallite size were found for the A_LaNi/Al sample compared to the Ni/Al sample, providing additional evidence of the La having some impact in the interaction between the Ni and the support.

Considerable disagreement was found between the average crystallite size estimated via pulsed H_2 chemisorption and the value derived from XRD (Table 1). The wide variation in average crystallite size cannot be solely attributed to uncertainties within the estimation techniques. A possible explanation for the difference may be via the occurrence of a Strong Metal Support Interaction-like (SMSI-like) effect between the dispersed La and Ni particles. That is, partially reduced LaO_x species, originating from the well-dispersed La_2O_3 on the support, may begin to decorate the surface of metallic Ni crystallites during the reduction at 700 °C, hindering H_2 adsorption at the blocked surface Ni sites and distorting the dispersion calculations. A depiction of the proposed SMSI-like effect is shown in Scheme 1a. An analogous SMSI-like effect was proposed by Zhang et al. who reported similar

discrepancies in Ni crystallite size estimation for a Ni/La_2O_3 catalyst reduced under H_2 at 500 °C [36]. Sánchez-Sánchez et al. also hinted at the decoration of metallic particles by dispersed species upon reducing a La-promoted Ni/Al catalyst at 700 °C [26].

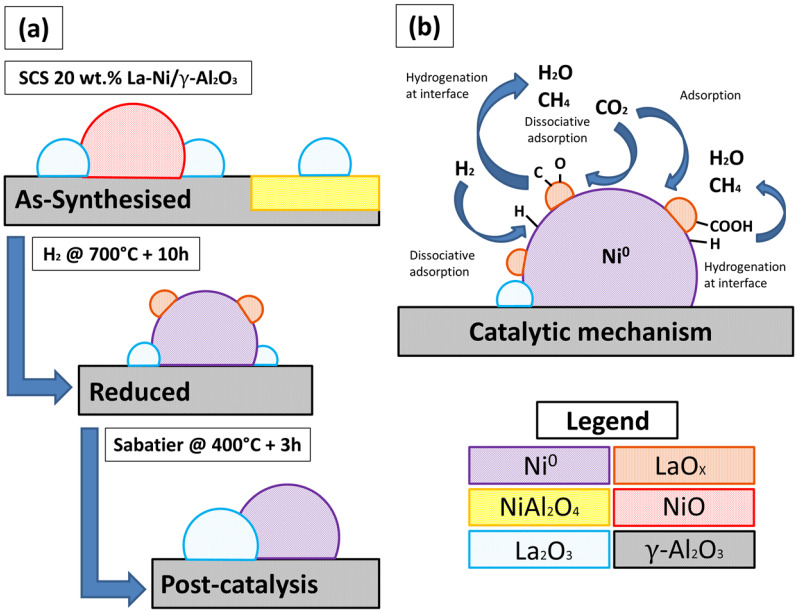

Scheme 1. Representation of the: (**a**) evolution of the La-Ni/γ-Al_2O_3 catalyst structure driven by SMSI-like (Strong Metal Support Interaction-like) effects promoted by La_2O_3; and (**b**) proposed catalytic reaction mechanism for CO_2 hydrogenation into CH_4.

Deconvoluted peaks for the Ni2p and La3d region of the A_LaNi/Al XPS spectrum are depicted in Figure 4a,b, respectively, with related information summarised in Table 2. Both the main and satellite Ni2p peaks were present at 854.24 and 860.95 eV, indicating the presence Ni^{2+} despite the catalyst undergoing a prior reduction step [21,26,27,30]. The presence of Ni^{2+} may derive from either: (i) La–O–Ni species at the interface between Ni crystallites and the LaO_x decoration (potentially formed during the reduction process); or (ii) surface NiO formed during re-oxidation of the metallic Ni during sample transfer to the XPS equipment.

The La3d signal for A_LaNi/Al appeared at 835.53 eV, representing a small shift towards lower binding energies (compared to 835.9 eV for P_LaNi/Al) but remaining within the range acceptable for surface La_2O_3. The 0.33 eV shift towards lower binding energies supports the notion of LaO_x decorating the Ni deposits as a 0.2 eV shift was reported by Fleisch et al. in a Pd/La_2O_3 system exhibiting SMSI effects [37]. Additionally, the increase in the $La3d_{5/2}$ satellite-split between the P_LaNi/Al and A_LaNi/Al samples (i.e., 3.57 to 3.73 eV) may endorse the proposed SMSI-like effect as they observed an analogous increase (i.e., from 3.3 to 3.8 eV) after reduction at 500 °C [37].

As shown in Table 2, a decrease in relative Ni/Al atomic ratio between the A_LaNi/Al and P_LaNi/Al samples indicates a loss in exposed Ni during the reduction at 700 °C. In contrast, no variation was seen for the relative La/Al ratio between the two materials signifying that La remained exposed during the reduction step. This loss of exposed Ni and the retention of exposed La further support the perception that La is decorating the Ni deposits during the reduction process.

2.3. Spent Catalyst (S_LaNi/Al)

The XRD pattern of the S_LaNi/Al (Figure 1) exhibited the reflections associated with the catalyst alumina support and the stainless steel sample holders. Metallic Ni reflections were also observed in the S_LaNi/Al XRD pattern, with a small relative increase in signal intensity being discernible

compared to the A_LaNi/Al counterpart. The increase in Ni diffraction peaks intensity may correspond to further reduction of remaining NiO during the catalytic process.

SEM imaging of the S_LaNi/Al sample (Figure 2d) revealed a surface mainly composed of aggregates (150–600 nm) and flake-like components evenly distributed across the catalyst particles. TEM micrographs (Figure 2e) revealed the presence of clearly discernible La/Ni particles with diameters between 4 and 9 nm (Table 1), uniformly distributed across the γ-Al_2O_3 support. None of the larger Ni deposit diameters (in the order of 20 nm) observed for A_LaNi/Al (Figure 2c) were readily observed for S_LaNi/Al suggesting a redistribution of the larger Ni deposits occurred during the reaction. EDS mapping (Figure 2f) confirmed that both La and Ni remained well-dispersed across the catalyst particle following reaction. No carbonaceous deposits were observed by TEM/SEM and associated EDS elemental mapping.

The impact of the Sabatier reaction on the Ni and La surface species, from XPS, is provided in Figure 4a,b, respectively, with associated details provided in Table 2. The Ni2p primary and satellite peaks for S_LaNi/Al occurred at 853.04 and 859.27 eV, respectively, which represented a shift towards lower binding energies compared to A_LaNi/Al and revealed the presence of surface metallic Ni [21,26]. No peaks corresponding to Ni^{2+} species were found for S_LaNi/Al, indicating that in-situ reduction of these species occurred during the course of the reaction. Abelló et al. reported a similar in-situ reduction in their study of a mixed-oxide NiO/Al_2O_3 catalyst for the Sabatier reaction [38]. They concluded that the Ni^{2+} that was reduced during reaction corresponded to NiO which had remained unreduced after the H_2 activation stage owing a certain level of sintering. In the case of S_LaNi/Al, though, the Ni^{2+} reduced in-situ is suspected to either comes from the NiO surface layer on the deposits and/or the possible La–O–Ni species observed in A_LaNi/Al. Reduction of surface NiO is supported by the small increase in intensity observed by XRD (Figure 1). The alternate hypothesis of La–O–Ni reduction is supported by a shift in the La3d peaks to 835.86 and 839.50 eV (Figure 4b), reverting to values similar to those observed for the P_LaNi/Al. This includes the satellite split which returned to a value of 3.57 eV. Accordingly, these results indicate that La is present as La_2O_3 after the reaction and provide evidence towards the disintegration of the proposed LaO_x decorations during reaction in agreement with the re-dispersion of the larger Ni particles observed by TEM (Figure 2b,c,e). A small decrease in the La/Al atomic ratio is also noted for S_LaNi/Al when compared to A_LaNi/Al (0.022 to 0.020, Table 2) and this also corroborates with the hypothesis of a disintegration of the LaO_x decorations, as previously hypothesized. No major changes were observed in the binding energies of the S_LaNi/Al XPS C1s components compared to those observed in P_LaNi/Al and A_LaNi/Al, (Supplementary Materials, Table S1). A depiction of the SMSI-like effect breakup leading to the re-dispersion of La and Ni at the surface of γ-Al_2O_3 is shown in Scheme 1a.

2.4. Catalyst Performance

Performance of the A_LaNi/Al catalyst for the Sabatier reaction over the range 200–400 °C is shown in Figure 5a in terms of CO_2 conversion and CH_4 selectivity. CO_2 conversion increased from <3% at 200 °C to ~80% at 350 °C. Selectivity towards CH_4 remained constant across the entire temperature range at values >98%. CO was the only secondary product detected from the hydrogenation reaction. Stability tests on A_LaNi/Al were conducted at 275 °C (Figure 5b) whereby, once stabilised, the CO_2 conversion remained steady at 65% with 98% selectivity towards CH_4 (pressure = 1 atm, H_2:CO_2 ratio = 4:1, GHSV = 7.2×10^4 mL·h^{-1}·g^{-1} cat., 20 wt % Ni loading). By comparison: (i) Ando et al. reported a 56% CO_2 conversion with 98% CH_4 selectivity at 300 °C for a neat $LaNi_5$ catalyst prepared by arc melting (pressure = 1 atm, H_2:CO_2 ratio = 4:1, WHSV = 3000 mL·h^{-1}·g^{-1} cat.) [18]; (ii) Liu et al. reported a 45% CO_2 conversion with 99% CH_4 selectivity at 300 °C for a Ni/Al_2O_3 catalyst prepared by impregnation (pressure = 1 atm, H_2:CO_2 ratio = 4:1, WHSV = 15,000 mL·h^{-1}·g^{-1} cat., 15 wt % Ni loading) [39]; and (iii) Abelló et al. reported a 8% CO_2 conversion with 95% CH_4 selectivity at 300 °C for a Ni_6Al (reduced) catalyst prepared by co-precipitation (pressure = 5 atm, H_2:CO_2 ratio = 4:1, WHSV = 26.88×10^5 mL·h^{-1}·g^{-1} cat., 69.1 wt % Ni loading) [38]. The stability profile also showed

that an initial induction period (~90 min) was needed prior to the catalyst reaching a stable and maximum activity. Although no direct evidence is available at this time, the induction period may account for the transformation of the LaO_x-decorated NiO into the reduced Ni/La_2O_3 form, which could be responsible for the higher catalyst activity. Irrespective of this and to our best knowledge, the P_LaNi/Al catalyst shows good performances as compared to other Ni-Al-based catalysts at a moderate temperature and ambient pressure.

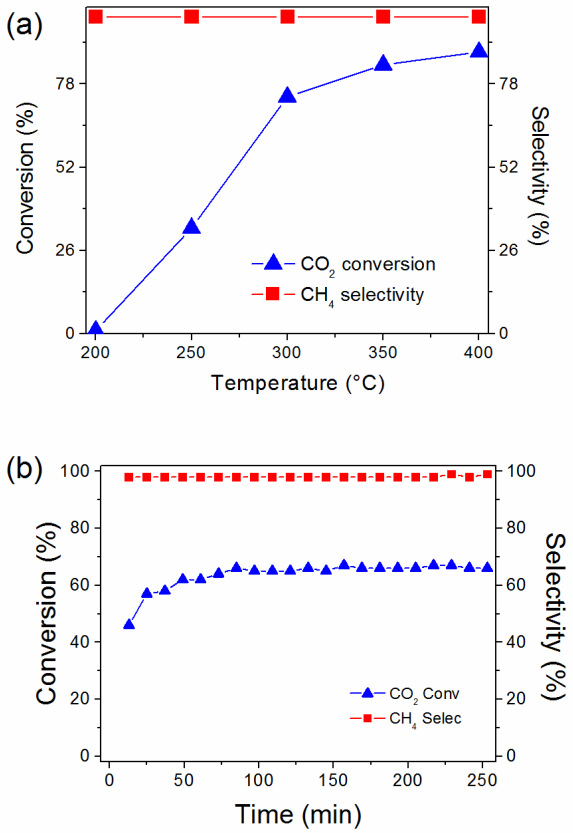

Figure 5. CO_2 conversion and CH_4 selectivity for the Sabatier reaction of A_LaNi/Al at: (**a**) temperatures ranging between 200 and 400 °C; and (**b**) at a constant temperature of 275 °C for 5 h.

The performance of the La-Ni/γ-Al_2O_3 catalyst prepared via SCS is postulated to derive from a combination of the SMSI-like effect and the physical-chemical promotional impact of La itself. According to the former, the formation of LaO_x decorations provided the catalytic system with La–O–Ni at the interface with the metallic Ni crystallites, which have been proposed to be highly active for the Sabatier reaction [40]. On the other hand, the promoting effects of La would be responsible for quicker/improved CO_2 dissociative adsorption due to its higher basicity [17,41–43] and better dispersion/stabilisation of the active Ni phase during preparation and reaction [27,44,45]. Interestingly, the post-reaction state of Ni and La in the catalyst differed to the activated.

2.5. Reaction Routes

An example of in-situ DRIFTS analysis profile for the La-Ni/γ-Al_2O_3 catalyst immediately following a H_2 pulse is provided in Figure 6a. The spectrum displays multiple bands between 1050 and 3010 cm^{-1}. The different species found at the surface of the catalyst during reaction include: $La_2O_2CO_3$ (1050 cm^{-1}) [46], unidentate formates on the Ni surface (1305 and 1607 cm^{-1}) [47], formates on the La_2O_3 surface (1350 and 1500 cm^{-1}) [40], bidentate formates on the γ-Al_2O_3 support (1375, 1395, 1590, and 3010 cm^{-1}) [47], adsorbed CO on Ni in bridge configuration (1860 and 1910 cm^{-1}) [47,48],

adsorbed CO on Ni in linear configuration (2030 cm^{-1}) [47,48], and adsorbed/gaseous CO_2 (2320 and 2360 cm^{-1}). Conversion of CO_2 into CH_4 during reaction was corroborated by the presence of the characteristic multi-peak bands observed at ca. 3100 and 1400 cm^{-1} with a strong peak at 3020 cm^{-1} corresponding to the Q-band of gaseous CH_4, while similar signals between 1200 and 2200 cm^{-1} indicated the presence of water.

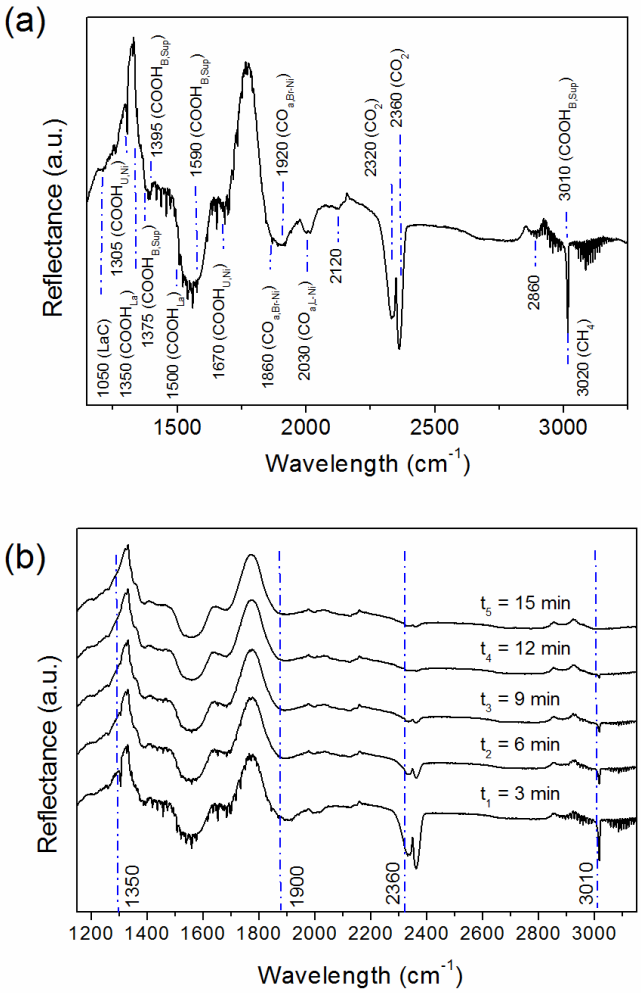

Figure 6. In-situ DRIFTS spectra of the A_LaNi/Al catalyst immediately following pulsed H_2 injection at 400 °C and 0.1 MPa over pre-adsorbed CO_2: (**a**) detailed account of the surface species present. LaC corresponds to $La_2O_2CO_3$, $COOH_{U,Ni}$ to unidentate formate on Ni, $COOH_{La}$ to formate on La_2O_3, $COOH_{B,Sup}$ to bidentate formate on the γ-Al_2O_3 support, $CO_{a,Br-Ni}$ to adsorbed CO_2 on Ni in a bridged configuration, and $CO_{a,L-Ni}$ to adsorbed CO_2 on Ni in a linear configuration; and (**b**) evolution of surface species as a function of time. The spectra correspond to the raw data and the "negative" features, e.g., at 15 min, are related to the slight differences between the diamond powder background and the spectrum of the catalyst diluted in diamond powder.

The evolution of surface species during the Sabatier reaction (400 °C and 0.1 MPa) is displayed by the consecutive in-situ DRIFTS spectra in Figure 6b. The monitored reflectance bands were those corresponding to unidentate formates over Ni, adsorbed CO on Ni in bridged configuration, adsorbed/gaseous CO_2, and bidentate formates on the γ-Al_2O_3 support. Results showed that gaseous/adsorbed CO_2 bands appeared right after the injection of H_2, indicating that H_2 preferentially adsorbed onto the catalyst and released part of the pre-adsorbed CO_2. Bands corresponding to water, methane, and formates on both Ni and the support were detected early within the reaction process (i.e.,

at t_1 = 3 min). As reaction time elapsed, the higher-amplitude signal corresponding to CO adsorbed on Ni in bridge configuration (1860 cm^{-1}) and the formates on the γ-Al_2O_3 support (3010 cm^{-1}) gradually disappeared. The Ni-bound formates disappeared quicker than those bound to the support, and were indiscernible after 9 min (t_3). The bands corresponding to the Ni adsorbed linear CO (2030 cm^{-1}) and the lower-amplitude bridged CO (1910 cm^{-1}), which were apparent 3 min after the first H_2 pulse (t_1), were not present after 6 min (t_2). After 15 min (t_5), some CO_2-related species remained adsorbed on the catalyst since the band at 2360 cm^{-1} was still present. After a second H_2 injection, the whole cycle was repeated and the presence of CO_2, remaining since the first H_2 injection, was corroborated.

On studying the hydrogenation of CO_2 into CH_4 over Ni/Al using FTIR and TPR, Fujita et al. identified different types of CO adsorbed on Ni in bridged position, proposing that the higher-amplitude band (i.e., 1860 cm^{-1}) corresponded to a strongly bound CO species while the lower-amplitude band (i.e., 1910 cm^{-1}) was related to weakly bound CO [47]. Additionally, formates present on the support and adsorbed CO species were presumed to undergo hydrogenation into CH_4 through a mechanism which involved further dissociation into adsorbed carbon, allowing for the amounts of adsorbed carbon and linear CO species to be negligible during reaction.

The results from in-situ DRIFTS appear to corroborate the presence and hydrogenation of formates and adsorbed CO strongly bound in a bridged configuration. Based on the findings by Fujita et al. [47] and accounting for the possible effects of LaO_x decorations on the catalyst as found in this work, a mechanism is proposed for the Sabatier reaction as follows: (a) dissociative adsorption of H_2 into H_{atomic} on Ni sites; (b) adsorption and hydrogen assisted cleavage of CO_2 on Ni sites; (c) dissociative adsorption of CO_2 onto LaO_x decorations; (d) cleavage of strongly adsorbed CO into adsorbed O and C; (e) hydrogenation of LaO_x-adsorbed CO over highly active La–O–Ni at the interface with the Ni crystallites; and (f) instantaneous hydrogenation of adsorbed C and O from adsorbed CO and formates into CH_4 and H_2O, respectively. The final step is consistent with the negligible carbon deposition on the S_LaNi/Al sample from XPS and TEM/SEM. A depiction of the previous reaction steps and the catalytic system is provided in Scheme 1b, where Ni- and γ-Al_2O_3-bound formates are represented since in-situ DRIFTS revealed their presence.

3. Materials and Methods

3.1. Catalyst Preparation

The Ni-La/γ-Al_2O_3 catalyst was prepared via solution combustion synthesis (SCS) using the corresponding metallic nitrates as oxidisers and glycine as the fuel/complexing agent [40]. A nickel nitrate ($Ni(NO_3)_2{\cdot}6H_2O$, Ajax Finechem Pty. Ltd., Sydney, Australia), lanthanum nitrate ($La(NO_3)_3{\cdot}6H_2O$, Merck KGaA, Sydney, Australia), and glycine ($C_2H_5O_2N$, Ajax Finechem Pty. Ltd., Sydney, Australia) solution was prepared at a fixed 1:5:6 molar ratio using deionised water as the solvent and keeping the overall combusting mixture under 500 mg. Once the nitrates and glycine had been dissolved, sufficient γ-Al_2O_3 (particle size 45–53 µm, Saint-Gobain NorPro, Japan) was added to the solution to give a nominal 20 wt % Ni-La loading on the final catalyst. The resulting slurry was stirred for 30 min and allowed to settle for a further 30 min after which it was transferred into a ceramic crucible and placed in a temperature controlled (±1 °C, FP21 Shimade Co., Ltd., Tokyo, Japan) muffle furnace. The SCS mixture was heated in the presence of air at 5 °C·min^{-1} from room temperature to 500 °C, calcined for 1 h, and then allowed to cool to room temperature. Control samples comprising 6.4 wt % La on γ-Al_2O_3 (La/Al) and 12.5 wt % Ni on γ-Al_2O_3 (Ni/Al) were also prepared using SCS.

3.2. Catalyst Characterisation

The La-Ni/γ-Al_2O_3 catalyst was characterised following preparation (P_LaNi/Al), activation (A_LaNi/Al) and post-reaction (i.e., spent following the Sabatier reaction at 400 °C for 3 h, S_LaNi/Al). P_LaNi/Al composition was determined by ICP-OES on a Perkin Elmer OPTIMA 7300 (Perkin Elmer, Sydney, Australia). Prior to analysis a small amount of the material was digested in concentrated

nitric acid (70 vol % HNO_3, Ajax Chem, Sydney, Australia) for 8 h at 80 °C and then diluted with de-ionised water.

Crystallinity of P_LaNi/Al, A_LaNi/Al and S_LaNi/Al was studied by X-ray Diffraction (XRD), using a Philips PANalytical X'pert Multipurpose XRD System (Phillips, Sydney, Australia) equipped with a monochromated Cu-Kα source (λ = 1.5418 Å), and operating at 45 kV and 40 mA.

Hydrogen temperature programmed reduction (H_2-TPR) analyses were performed on a Micromeritics Autochem II 2920 (Micromeritics, Sydney, Australia) to assess the reducibility of P_LaNi/Al catalyst as well as the control materials. Materials were pre-treated by flowing argon through the bed at 120 °C for 30 min and then cooled to 50 °C. Then, 10 vol % H_2/Ar was passed over the catalyst bed while the temperature was increased at 5 °C·min^{-1} from 50 to 800 °C.

Pulsed H_2 chemisorption assays were conducted to estimate the Ni dispersion and crystallite size for P_LaNi/Al and Ni/Al using a Micromeritics Autochem II 2920. The materials were initially pre-treated by flowing argon through the bed at 120 °C for 30 min after which they were cooled to room temperature. Pure hydrogen was passed through the sample bed as the temperature was increased at 10 °C·min^{-1} up to 700 °C where it was held for 5 h. The system was subsequently flushed with argon for 2 h at 700 °C and cooled to room temperature. Consecutive volumetric pulses (0.4664 mL) of 10 vol % H_2/Ar were then dosed to the sample every 1.5 min. Ni dispersion and crystallite size were estimated assuming an atomic ratio of 1 between adsorbed atomic hydrogen and surface Ni at room temperature [20,36,49] and by following the procedure proposed by Bartholomew et al. [50].

Scanning Electron Microscopy (SEM) analyses were carried out using a FEI Nova Nano-SEM 230 FESEM instrument (FEI, Sydney, Australia), while Transmission Electron Microscopy (TEM) and energy-dispersive X-ray spectroscopy (EDS) studies were performed on a Philips CM200 FEG TEM (Phillips, Sydney, Australia) equipped with an interfaced EDAX system (Phillips, Sydney, Australia) and operated at 200 keV.

Chemical characteristics and relative atomic compositions of the P_LaNi/Al, A_LaNi/Al and S_LaNi/Al catalyst surfaces were studied by XPS using a Thermo ESCALAB250i XPS instrument (Thermo Scientific, Sydney, Australia) equipped with a monochromated Al-Kα X-ray source and powered at 13 kV/12 mA. Adventitious hydrocarbon, C1s (285.0 eV), was used as the binding energy (BE) reference. Air sensitive samples were prepared in a glove box (LC Technology, Salisbury, MD, USA) under high purity argon immediately prior to XPS analysis to minimise the potential of oxidation.

3.3. Catalytic Assessment

Catalytic activity tests for the Sabatier reaction were conducted in a continuous-flow fixed-bed reactor (6 mm ID quartz tube, (CGB, Sydney, Australia)) equipped with both temperature and mass flow controllers (H_2 and N_2: Brooks Sydney, Australia; CO_2: Aalborg, Sydney, Australia). Prior to each catalytic test, 0.05 g of the catalyst was reduced in-situ for 3 h using 50% hydrogen in nitrogen at 60 mL·min^{-1} and 700 °C. A stoichiometric mixture of H_2/CO_2 (i.e., 4:1 molar ratio) was fed into the system at a 7.2 × 10^4 mL·h^{-1}·g^{-1} cat. GHSV, with hydrogen and carbon dioxide (Coregas, Sydney, Australia) flowing at 40 and 10 mL·min^{-1}·g^{-1} cat. STP, respectively. Reaction temperatures were varied between 150 and 450 °C. The product gas was analysed with an on-line gas chromatograph (Shimadzu GC-2010 Plus, Shimadzu, Sydney, Australia) equipped with a TCD and Agilent CarboPlot P7 column (Agilent, Sydney, Australia), and an FID and methaniser, and used argon (Coregas, Sydney, Australia) as the carrier gas. The reaction was then stopped, the reactor cooled under flowing H_2/CO_2, and the spent catalyst samples collected/stored in sealed Ar-filled vials for further analysis. Catalyst stability was also assessed by running the reaction under the conditions described above at 275 °C for 5 h.

The evolution of surface species during CO_2 hydrogenation was followed using in-situ Diffuse Reflectance Infrared Fourier Transform Spectroscopy (DRIFTS) (Harrick, New York, NY, USA). Prior to measurements, the catalyst was activated in-situ as per conditions above. Spectra were collected using a Brüker VERTEX 70v FTIR spectrometer (Bruker, Sydney, Australia) and equipped with a commercial

in-situ DRIFTS cell (Harrick's Scientific, Ithaca, NY, USA). For each analysis, approximately 20 mg of the activated catalyst (A_LaNi/Al) was diluted with synthetic mono-crystalline diamond powder (~1 μm, Sigma-Aldrich, Sydney, Australia). Operating conditions within the sample cell were set at 400 °C and 0.1 MPa. Prior to analysis, the cell was flushed with argon for 30 min at 150 °C. Carbon dioxide was then fed for 30 min into the reaction chamber at 400 °C and allowed to adsorb onto the activated catalyst. The pre-adsorbed CO_2 was reacted with H_2 by dosing ~20 mL injections every 3 min and the evolution of surface species during reaction was followed.

4. Conclusions

A LaNi/γ-Al_2O_3 catalyst, synthesised using SCS, exhibited good activity for the Sabatier reaction at atmospheric pressure, reaching CO_2 conversions of ~80% at temperatures of 350 °C and beyond and a CH_4 selectivity consistently >98%. Characterisation of the LaNi/γ-Al_2O_3 catalyst at various stages of the reaction process (i.e., as-prepared, activated and post-reaction) demonstrated the La and Ni existed in different forms at each stage. La and Ni in the as-prepared catalyst were observed to be present as amorphous surface La–Ni spinels. The activation process did not reduce the Ni as anticipated, rather it appeared to promote the formation of oxidised Ni particles (i.e., Ni^{2+}) decorated with LaO_x moieties. The reaction conditions led to the in-situ reduction of the Ni (to give metallic Ni deposits) with the LaO_x species returning to an oxidation state (La_2O_3) similar to that observed for the as-prepared catalyst. At the interface between LaO_x decorations and the Ni crystallites, La–O–Ni species may be present which could potentially be accountable for the catalyst activity, although the change in catalyst characteristics during the reaction in conjunction with the stable activity of the catalyst imply that the activated catalyst may be an intermediary state of the ultimately active material. In-situ DRIFTS analyses revealed the presence of adsorbed formates and adsorbed CO species during reaction at 400 °C. The results suggested that the reaction advanced through a CO-based mechanism involving CO_2 hydrogenation, although the pathway involving the hydrogenation of formates cannot be excluded. The findings demonstrate the capacity for hydrogen storage based materials, such as LaNi alloys, to behave as active catalysts for the Sabatier reaction in this instance, and potentially for other hydrogenation reactions in general, when loaded on a metal oxide support.

Supplementary Materials: The following are available online at www.mdpi.com/2073-4344/6/11/170/s1, Figure S1: X-ray Photoelectron (XPS) spectra and curve fitting of P_LaNi/Al, A_LaNi/Al and S_LaNi/Al at the C1s region, Figure S2: X-ray photoelectron spectra and curve fitting of P_LaNi/Al, A_LaNi/Al and S_LaNi/Al at the Ni2p and La3d region, Figure S3: X-ray photoelectron spectra of the P_LaNi/Al at the (a) O1s and (b) Al2p regions, Figure S4. TEM images and (f) associated elemental mapping of A_LaNi/Al, Table S1: Carbon (C1s) binding energies (BEs) of core electrons, surface species and relative Ci/Al atomic ratio for the P_LaNi/Al, A_LaNi/Al, and S_LaNi/Al.

Acknowledgments: The authors would also like to acknowledge the use of facilities within the UNSW Mark Wainwright Analytical Centre and Bill Bin Gong for assistance with the XPS analyses, also located within the UNSW Mark Wainwright Analytical Centre.

Author Contributions: Daniel E. Rivero-Mendoza carried out all the experimental work which was conceived and designed with Jason Scott and Kondo-François Aguey-Zinsou. Jessica N. G. Stanley, conducted the stability test. All contributed to the writing of the manuscript.

Conflicts of Interest: The authors declare no conflict of interest.

References

1. Susan, S. *Climate Change 2007—The Physical Science Basis: Working Group I Contribution to the Fourth Assessment Report of the IPCC*; Cambridge University Press: Cambridge, UK, 2007.
2. Tans, P.; Keeling, R. *Trends in Atmospheric Carbon Dioxide*; NOAA Earth System Research Laboratory: Boulder, CO, USA, 2014.
3. Wang, W.; Wang, S.; Ma, X.; Gong, J. Recent advances in catalytic hydrogenation of carbon dioxide. *Chem. Soc. Rev.* **2011**, *40*, 3703–3727. [CrossRef] [PubMed]

4. Wei, W.; Jinlong, G. Methanation of carbon dioxide: an overview. *Front. Chem. Sci. Eng.* **2011**, *5*, 2–10. [CrossRef]
5. Centi, G.; Perathoner, S. Opportunities and prospects in the chemical recycling of carbon dioxide to fuels. *Catal. Today* **2009**, *148*, 191–205. [CrossRef]
6. Hunt, A.J.; Sin, E.H.K.; Marriott, R.; Clark, J.H. Generation, capture, and utilization of industrial carbon dioxide. *ChemSusChem* **2010**, *3*, 306–322. [CrossRef] [PubMed]
7. Zhilyaeva, N.A.; Volnina, E.A.; Kukina, M.A.; Frolov, V.M. Carbon dioxide hydrogenation catalysts (a review). *Petrol. Chem.* **2002**, *42*, 367–386.
8. Chang, F.-W.; Kuo, M.-S.; Tsay, M.-T.; Hsieh, M.-C. Hydrogenation of CO_2 over nickel catalysts on rice husk ash-alumina prepared by incipient wetness impregnation. *Appl. Catal. A Gen.* **2003**, *247*, 309–320. [CrossRef]
9. Ibraeva, Z.A.; Nekrasov, N.V.; Gudkov, B.S.; Yakerson, V.I.; Beisembaeva, Z.T.; Golosman, E.Z.; Kiperman, S.L. Kinetics of methanation of carbon dioxide on a nickel catalyst. *Theor. Exp. Chem.* **1991**, *26*, 584–588. [CrossRef]
10. Yamasaki, M.; Habazaki, H.; Yoshida, T.; Akiyama, E.; Kawashima, A.; Asami, K.; Hashimoto, K.; Komori, M.; Shimamura, K. Compositional dependence of the CO_2 methanation activity of Ni/ZrO_2 catalysts prepared from amorphous NiZr alloy precursors. *Appl. Catal. A Gen.* **1997**, *163*, 187–197. [CrossRef]
11. Weatherbee, G.D.; Bartholomew, C.H. Hydrogenation of CO_2 on group VIII metals. I. Specific activity of Ni/SiO_2. *J. Catal.* **1981**, *68*, 67–76.
12. Solymosi, F.; Erdöhelyi, A.; Bánsági, T. Methanation of CO_2 on supported rhodium catalyst. *J. Catal.* **1981**, *68*, 371–382. [CrossRef]
13. Lunde, P.J.; Kester, F.L. Rates of methane formation from carbon dioxide and hydrogen over a ruthenium catalyst. *J. Catal.* **1973**, *30*, 423–429. [CrossRef]
14. Novák, É.; Fodor, K.; Szailer, T.; Oszkó, A.; Erdöhelyi, A. CO_2 hydrogenation on Rh/TiO_2 previously reduced at different temperatures. *Top. Catal.* **2002**, *20*, 107–117. [CrossRef]
15. Park, J.-N.; McFarland, E.W. A highly dispersed $Pd–Mg/SiO_2$ catalyst active for methanation of CO_2. *J. Catal.* **2009**, *266*, 92–97. [CrossRef]
16. Solymosi, F.; Erdöhelyi, A. Hydrogenation of CO_2 to CH_4 over alumina-supported noble metals. *J. Mol. Catal.* **1980**, *8*, 471–474. [CrossRef]
17. Ando, H.; Fujiwara, M.; Matsumura, Y.; Miyamura, H.; Souma, Y. Methanation of carbon dioxide over $LaNi_4X$ type catalysts. *Energy Convers. Manag.* **1995**, *36*, 653–656. [CrossRef]
18. Ando, H.; Fujiwara, M.; Matsumura, Y.; Tanaka, M.; Souma, Y. Catalytic hydrogenation of carbon dioxide over $LaNi_5$ activated during the reaction. *J. Mol. Catal. A Chem.* **1999**, *144*, 117–122. [CrossRef]
19. Scheffer, B.; Heijeinga, J.J.; Moulijn, J.A. An electron spectroscopy and X-ray diffraction study of nickel oxide/alumina and nickel-oxide-tungsten trioxide/alumina catalysts. *J. Phys. Chem.* **1987**, *91*, 4752–4759. [CrossRef]
20. Bartholomew, C.H.; Pannell, R.B. The stoichiometry of hydrogen and carbon monoxide chemisorption on alumina and silica supported nickel. *J. Catal.* **1980**, *65*, 390–401. [CrossRef]
21. Kirumakki, S.R.; Shpeizer, B.G.; Sagar, G.V.; Chary, K.V.R.; Clearfield, A. Hydrogenation of naphthalene over $NiO/SiO_2–Al_2O_3$ catalysts: Structure–activity correlation. *J. Catal.* **2006**, *242*, 319–331. [CrossRef]
22. Li, C.; Chen, Y.-W. Temperature-programmed-reduction studies of nickel oxide/alumina catalysts: Effects of the preparation method. *Thermochim. Acta* **1995**, *256*, 457–465. [CrossRef]
23. Poncelet, G.; Centeno, M.A.; Molina, R. Characterization of reduced α-alumina-supported nickel catalysts by spectroscopic and chemisorption measurements. *Appl. Catal. A Gen.* **2005**, *288*, 232–242. [CrossRef]
24. Tsai, W.; Schwarz, J.A.; Driscoll, C.T. Differential cation exchange capacity (DCEC) of nickel supported on silica-aluminas. *J. Catal.* **1982**, *78*, 88–95. [CrossRef]
25. Barros, B.S.; Melo, D.M.A.; Libs, S.; Kiennemann, A. CO_2 reforming of methane over $La_2NiO_4/α\text{-}Al_2O_3$ prepared by microwave assisted self-combustion method. *Appl. Catal. A Gen.* **2010**, *378*, 69–75. [CrossRef]
26. Sánchez-Sánchez, M.C.; Navarro, R.M.; Fierro, J.L.G. Ethanol steam reforming over $Ni/La–Al_2O_3$ catalysts: Influence of lanthanum loading. *Catal. Today* **2007**, *129*, 336–345. [CrossRef]
27. Yang, R.; Li, X.; Wu, J.; Zhang, X.; Zhang, Z. Promotion Effects of copper and lanthanum oxides on nickel/gamma-alumina catalyst in the hydrotreating of crude 2-ethylhexanol. *J. Phys. Chem. C* **2009**, *113*, 17787–17794. [CrossRef]
28. Scheffer, B.; Molhoek, P.; Moulijn, J.A. Temperature-programmed reduction of $NiOWO_3/Al_2O_3$ hydrodesulphurization catalysts. *Appl. Catal.* **1989**, *46*, 11–30. [CrossRef]

29. Mordovin, V.P.; Kasimtsev, A.V.; Alekhin, V.P.; Zhigunov, V.V. Industrial technologies for production of $LaNi_5$-based hydride materials. In *Hydrogen Materials Science and Chemistry of Carbon Nanomaterials*; Veziroglu, T.N., Zaginaichenko, S., Schur, D., Baranowski, B., Shpak, A., Skorokhod, V., Kale, A., Eds.; Springer: Dordrecht, The Netherlands, 2007; pp. 407–414.
30. Bunch, A.Y.; Wang, X.; Ozkan, U.S. Hydrodeoxygenation of benzofuran over sulfided and reduced Ni–Mo/γ-Al_2O_3 catalysts: Effect of H_2S. *J. Mol. Catal. A Chem.* **2007**, *270*, 264–272. [CrossRef]
31. Damyanova, S.; Daza, L.; Fierro, J.L.G. Surface and catalytic properties of lanthanum-promoted Ni/sepiolite catalysts for styrene hydrogenation. *J. Catal.* **1996**, *159*, 150–161. [CrossRef]
32. Légaré, P.; Fritsch, A. XPS study of transition metal/alumina model catalysts: Equilibrium and energy referencing. *Surf. Interface Anal.* **1990**, *15*, 698–700. [CrossRef]
33. Salvati, L.; Makovsky, L.E.; Stencel, J.M.; Brown, F.R.; Hercules, D.M. Surface spectroscopic study of tungsten-alumina catalysts using X-ray photoelectron, ion scattering, and raman spectroscopies. *J. Phys. Chem.* **1981**, *85*, 3700–3707. [CrossRef]
34. Tanabe, T.; Asaki, Z. Formation mechanism of $LaNi_5$ in the reduction-diffusion process. *Metall. Mater. Trans. B* **1998**, *29*, 331–338. [CrossRef]
35. Yasuda, N.; Tsuchiya, T.; Sasaki, S.; Okinaka, N.; Akiyama, T. Self-ignition combustion synthesis of $LaNi_5$ at different hydrogen pressures. *Int. J. Hydrog. Energy* **2011**, *36*, 8604–8609. [CrossRef]
36. Zhang, Z.; Verykios, X.E. Carbon dioxide reforming of methane to synthesis gas over Ni/La_2O_3 catalysts. *Appl. Catal. A Gen.* **1996**, *138*, 109–133. [CrossRef]
37. Fleisch, T.H.; Hicks, R.F.; Bell, A.T. An XPS study of metal-support interactions on $PdSiO_2$ and $PdLa_2O_3$. *J. Catal.* **1984**, *87*, 398–413. [CrossRef]
38. Abelló, S.; Berrueco, C.; Montané, D. High-loaded nickel–alumina catalyst for direct CO_2 hydrogenation into synthetic natural gas (SNG). *Fuel* **2013**, *113*, 598–609. [CrossRef]
39. Liu, H.; Zou, X.; Wang, X.; Lu, X.; Ding, W. Effect of CeO_2 addition on Ni/Al_2O_3 catalysts for methanation of carbon dioxide with hydrogen. *J. Nat. Gas Chem.* **2012**, *21*, 703–707. [CrossRef]
40. González-Cortés, S.L.; Imbert, F.E. Fundamentals, properties and applications of solid catalysts prepared by solution combustion synthesis (SCS). *Appl. Catal. A Gen.* **2013**, *452*, 117–131. [CrossRef]
41. Barrault, J.; Guilleminot, A.; Percheron-Guegan, A.; Paul-Boncour, V.; Achard, J.C. Olefin hydrogenation over some $LaNi_5{-}xM_x$ intermetallic systems. *Appl. Catal.* **1986**, *22*, 263–271. [CrossRef]
42. Inui, T. Highly effective conversion of carbon dioxide to valuable compounds on composite catalysts. *Catal. Today* **1996**, *29*, 329–337. [CrossRef]
43. Tsipouriari, V.A.; Verykios, X.E. Carbon and oxygen reaction pathways of CO_2 reforming of methane over Ni/La_2O_3 and Ni/Al_2O_3 catalysts studied by isotopic tracing techniques. *J. Catal.* **1999**, *187*, 85–94. [CrossRef]
44. Cui, Y.; Zhang, H.; Xu, H.; Li, W. The CO_2 reforming of CH_4 over Ni/La_2O_3/α-Al_2O_3 catalysts: The effect of La_2O_3 contents on the kinetic performance. *Appl. Catal. A Gen.* **2007**, *331*, 60–69. [CrossRef]
45. Martínez, R.; Romero, E.; Guimon, C.; Bilbao, R. CO_2 reforming of methane over coprecipitated Ni–Al catalysts modified with lanthanum. *Appl. Catal. A Gen.* **2004**, *274*, 139–149. [CrossRef]
46. Verykios, X.E. Catalytic dry reforming of natural gas for the production of chemicals and hydrogen. *Hem. Ind.* **2002**, *56*, 238–255. [CrossRef]
47. Fujita, S.-I.; Nakamura, M.; Doi, T.; Takezawa, N. Mechanisms of methanation of carbon dioxide and carbon monoxide over nickel/alumina catalysts. *Appl. Catal. A Gen.* **1993**, *104*, 87–100. [CrossRef]
48. Zakumbaeva, G.D.; Urumbaeva, S.U.; Nigmetova, D.T.; Khisametdinov, A.M.; Kuanyshev, A.S. CO_2 hydrogenation on iron-containing mono- and bimetallic catalysts. *React. Kinet. Catal. Lett.* **1987**, *34*, 123–128. [CrossRef]
49. Lansink Rotgerink, H.G.J.; Slaa, J.C.; van Ommen, J.G.; Ross, J.R.H. Studies on the promotion of nickel-Alumina coprecipitated catalysts: III. Cerium oxide. *Appl. Catal.* **1988**, *45*, 281–290. [CrossRef]
50. Bartholomew, C.H.; Pannell, R.B.; Butler, J.L. Support and crystallite size effects in CO hydrogenation on nickel. *J. Catal.* **1980**, *65*, 335–347. [CrossRef]